USING BAYESIAN INFERENCE TO IMPROVE THE ANALYTICAL EAGAR-TSAI MODEL WITH IMPLICATIONS IN THE ADDITIVE MANUFACTURING OF METALS

Author: Brendan Whalen [a,b]
bjw2qwf@virginia.edu

Advisor: Dr. Prasanna Balachandran [a,b,c]
pvb5e@virginia.edu

[a] University of Virginia
[b] Department of Mechanical and Aerospace Engineering
[c] Department of Materials Science Engineering

Abstract: *This paper focuses on improving melt pool geometry predictions in the laser powder bed fusion (L-PBF) process using an adapted version of the analytical Eagar-Tsai (E-T) model. Temperature dependent properties of the material and powder bed conditions are incorporated into the conventional E-T model as derived for metal arc welding. Through the incorporation of experimental results into the analysis, the novel statistical method of Bayesian inference is employed to predict distributions for the adapted E-T model input parameters as a function of laser power and speed. This analysis is performed for a variety of material systems, including Inconel 718, 316L stainless steel, and Ti-6Al-4V. Although conventionally treated as constant values in simulations and modeling, our Bayesian inference results suggest that the absorptivity and powder bed porosity are highly influenced by laser power and scanning speed. To demonstrate the merits of this approach, material specific printability maps are constructed using the Bayesian fit adapted E-T model which now predicts the lack of fusion and keyhole regions typically out of the scope of the conventional E-T model.*

Keywords: Additive manufacturing · Bayesian inference · Eagar-Tsai model · Laser powder bed fusion (L-PBF) · Printability Map

Introduction

Laser powder bed fusion (L-PBF) is an additive manufacturing process that uses layer-by-layer fusion of a metallic powder bed to create complex, fully dense 3D parts. In this process the laser is set to scan the powder layer at a specific power and speed depending on the material and desired properties. As the process becomes more developed, applications in many sectors are increasing in importance and scale, particularly in the aerospace and medical industries. Despite large advances in L-PBF machines and processes in recent years, variability in the outcome has yet to be fully explored and the qualification of additively manufactured parts continues to be a serious hurdle to widespread adoption.[1] Any residual porosity and defects that arise can seriously degrade the mechanical properties of the finished part and the lack of repeatability in the quality of finished parts is a large barrier to the transition from L-PBF in the production of prototypes to the production of critical parts at scale.[2] Understanding the boundaries of the parameter space, where parts can be printed successfully, is thus of critical importance to reliably and repeatedly produce parts without defects.

Akin to phase diagrams in materials science, there is a growing interest in constructing material printability maps from numerical and/or data-driven models that illustrate the influence of processing parameters, such as laser power and scan speed, on build defects. These maps generally demarcate melt pool morphologies into four regions: keyhole, lack of fusion, balling and conduction.[3-5] The conduction mode region is the desired melt pool morphology because it promotes fully dense parts. Constructing reliable printability maps is a non-trivial task, because there are many commercially available L-PBF systems, each of which occupies a distinct part of the L-PBF parameter space. The multitude of parameters that the L-PBF process is dependent on can largely be grouped into three categories: laser parameters, material properties and powder bed conditions. Among these parameters, laser power and speed are generally considered the two most important process parameters and have been studied most extensively to date.[6]

Numerous approaches to modeling the L-PBF process, as well as methods of in-situ observation, have been developed and implemented. These are used to better understand the process and provide recommendations for controllable parameters to ensure the highest quality of parts while minimizing the need for expensive physical experimentation. Modeling methods range from high-fidelity finite element analysis simulations that require super-computing resources to semi-analytical or numerical models that can be run on a personal laptop in a matter of minutes.[3] Selecting which model to use for a given application typically depends on the purpose of the investigation and the desired accuracy

of the results. One such analytical model is that derived by Eagar & Tsai (E-T) for application to metal arc fusion welding, but it has also been widely applied to the L-PBF process as a relatively simple model for predicting the resulting temperature distribution and melt pool dimensions for a given set of process parameters.[7] Applying this model to L-PBF is limited by the differences between metal arc welding and L-PBF. The model assumes a quasi-steady state semi-infinite medium and constant average thermal properties of the material in addition to ignoring the physical phenomena of evaporation, recoil pressure, and Marangoni convection.[8] Despite its limitations, the E-T model remains a valuable resource for quickly exploring the L-PBF parameter space, where it can be used to determine under what conditions the desired melt pool geometry might be attained.[8] The presence of a wide range of process parameters makes experimentation and high-fidelity physics-based simulations prohibitively expensive to rapidly explore the entire parameter space. When appropriately implemented and calibrated, the E-T model can serve as a low-cost alternative to guide experiments.[1,8-10]

Methods

In this work, the analytical solution to the original E-T model is modified in two ways. First, temperature dependence of the material properties and powder conditions are incorporated as shown in Fig. 1. The powder bed conditions are incorporated through the use of effective values for certain medium properties that are parameters of the E-T model. Specifically, effective values are calculated for the density and thermal conductivity of a powder bed, which can vary substantially when considering the packing of a powder layer as opposed to a solid.

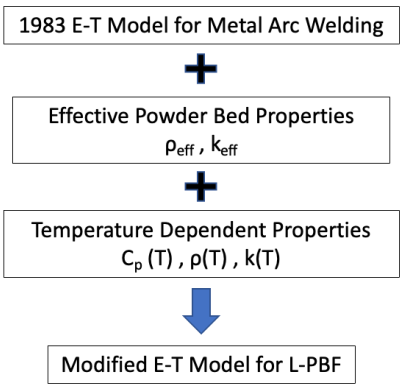

Fig. 1 Modifications made to the original 1983 E-T model for application to the L-PBF process

Second, a novel type of statistical analysis called Bayesian inference is used to fit the modified model to the experimental data through the process shown in Fig. 2.[11] This is accomplished by determining viable distributions for the effective absorptivity and powder bed porosity input parameters. While the original E-T model is dependent on laser power and scan speed, the Bayesian fit E-T model in this paper is also dependent on the effective material absorptivity and powder packing density, in addition to the temperature dependence of the specific heat, thermal conductivity and density material properties. The Bayesian fit input parameters are interpolated across the parameter space and used to predict the resulting melt pool geometry for a given power and speed. The outputs of the Bayesian E-T model are the primary melt pool dimensions of depth and width, which are used to geometrically classify a given melt pool geometry as producing defects or not in the construction of material-specific printability maps.

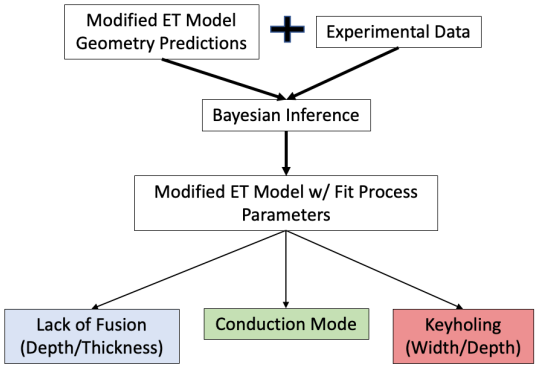

Fig. 2 Illustration of the Bayesian inference process

For this research, the choice was made to use several commonly used material systems to demonstrate the efficacy of this computational approach across the material space used in L-PBF. While the model can theoretically be fit to any material, the material properties of interest may not be available in literature and there may be a limited amount of experimental data for the fitting process. For this reason, the materials of 316L stainless steel, Ti-6Al-4V, and Inconel 718 were used to fit the model. For all three of these materials, there is extensive publicly available literature on single track experiments that is used as the source of experimentally determined melt pool geometry data for the Bayesian inference process.

Modified E-T Model for L-PBF

The dimensionless solution, presented by Eagar & Tsai, for the temperature field produced by a distributed traveling heat source is shown in Eqs. 1-3 with terms as defined in Table 1.[7] The output of the E-T model is a 3D matrix of temperature values for given locations in the x-y-z coordinate system. Characteristics of the melt pool geometry are determined by the boundaries of where the local temperature is greater than the material melting

point. An implementation of this model is coded in the R computing language.

$$\boldsymbol{\theta} = \frac{\boldsymbol{n}}{\sqrt{2\pi}} \int_0^{\frac{v^2 t}{2a}} \boldsymbol{d\tau} \frac{\tau^{\frac{-1}{2}}}{\tau + u^2} \quad \boldsymbol{e}^{-\frac{\xi^2+\psi^2+2\xi\tau+\tau^2}{2\tau+2u^2} - \frac{\zeta^2}{2\tau}} \tag{1}$$

$$\boldsymbol{\xi} = \frac{vw}{2a}, \ \boldsymbol{\psi} = \frac{vy}{2a}, \ \boldsymbol{\zeta} = \frac{vz}{2a}, \ \boldsymbol{\tau} = \frac{v^2 t''}{2a} \tag{2}$$

$$\boldsymbol{\theta} = \frac{T - T_0}{T_c - T_0}, \ \boldsymbol{n} = \frac{qv}{4\pi a^2 \rho c_p (T_c - T_0)}, \ \boldsymbol{u} = \frac{v\sigma}{2a} \tag{3}$$

Table 1 List of symbols and definitions used in the E-T solution

Symbol	Definition
a	Thermal diffusivity
c_p	Specific heat capacity at constant pressure
n	Operating parameter
q	Net heat input (power)
T	Temperature
T_0	Initial temperature
T_c	Critical temperature (melting temperature)
u	Dimensionless distribution parameter
v	Travel speed of laser arc
w	Distance in x direction in a moving coordinate
y	Distance in y direction
z	Distance in z direction
σ	Distribution parameter
ρ	Density
τ	Dimensionless time
θ	Dimensionless temperature
ξ	Dimensionless distance in the moving coordinate
ψ	Dimensionless distance y
ζ	Dimensionless distance z

Although not used as explicit parameters in the solution, the source laser power is multiplied by the effective absorptivity to calculate the net laser power absorbed by the material and the powder bed porosity is considered in the calculation of effective density and thermal conductivity. The effective absorptivity and powder bed porosity parameters are of particular interest in the improvement of the E-T model. These two parameters can vary widely, are often unknown and are arguably the most difficult to measure using in-situ techniques.[12-14]

A numerical value for laser absorptivity is defined as the ratio between absorbed and incident energy.[15] Direct measurement of the absorption of laser light by metal powder is quite difficult and can be attributed to the absorptivity's dependence on numerous factors such as the powder properties, beam profile and even the layer thickness. In L-PBF, the absorption is highly non-uniform even on the scale of the individual powder particles.[16] Given some ambiguity in the physical meaning of the absorptivity parameter that enters the low-fidelity E-T model, it is referred to as effective absorptivity.

The powder packing density can vary from location to location in the powder bed, and when laser interactions are considered on the scale of the individual particles, the variation can be a significant factor. Powder bed porosity, which is the complement of packing density, affects numerous material properties, such as the effective density, thermal conductivity and laser absorption. Represented by ϕ, powder bed porosity is the ratio of the volume of the interstitial voids to the total volume. Effective density of the powder bed can thus be calculated to be $\rho_{eff} = (1 - \phi) * \rho_{solid}$. Under the assumption that the gas does not absorb any of the laser radiation, the specific heat capacity of the powder is taken to be that of the fully dense solid. The effect of the powder conditions on the thermal conductivity is considered by use of the Lewis-Nielson (L-N) model.[17,18] While the E-T model fails to account for the complex phenomena of recoil momentum and evaporation that lead to the formation of vapor depressions, it is believed that the variations in the local packing density can act as a surrogate to capture some of these effects.

Experimental Data

Extensive experimental melt pool geometry data is gathered from published single-track scan studies.[1,10,19-25] For each material investigated, data is available across the viable laser power and scan speed (P-V) process space that is typical for L-PBF. In these experiments, the laser scans a single line at various power and speed combinations and the resulting samples are cut and analyzed to determine the melt pool width and depth from the scan line cross-section. Of the measured melt pool dimensions, the depth is of greatest interest as it indicates if the energy is sufficient to melt through the powder to the substrate and if the melt pool penetrates too deep which is associated with keyholing defects.[1] Therefore, the Bayesian fitting process was performed with the measured melt pool depth.

In order to infer parameter values according to the different processing conditions at which the experimental data is gathered, it is necessary to partition the experimental data according to the power and speed used. For this, 16 partitions of equal size were created from the experimental data based on data points having similar power and speed. The partitioning scheme is visualized in Figs. 3 & 4 of the raw Ti-6Al-4V data and the partitioned data. The described Bayesian inference routine for effective absorptivity and porosity parameters was performed for each partition and for each material. Future work will focus on utilizing a larger dataset from consistent experiments. It should be noted that when more data become available, the Bayesian E-T model can be re-trained to further refine the parameter distributions and improve the relative positions of the

boundaries that separate the various regions in the printability map. The adaptive approach is attractive and a desired one, especially given the large variability in the melt pool measurements.

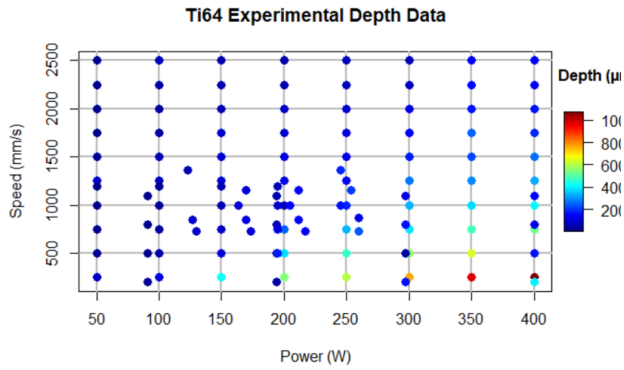

Fig. 3 Plot of the raw experimental single track depth data for Ti-6Al-4V

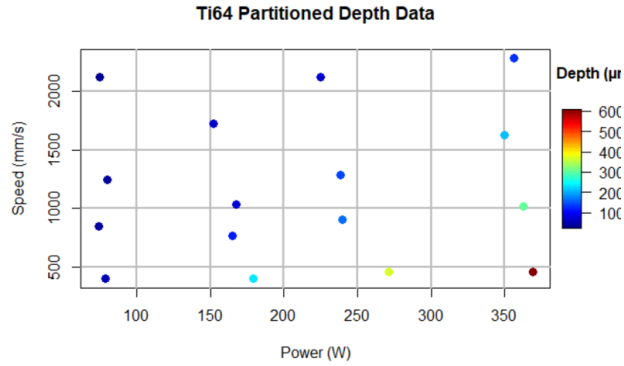

Fig. 4 Plot of the mean depth of each partitioned data set from the experimental Ti-6Al-4V data

Bayesian Inference

Bayesian methods start with existing information about model parameters in the form of a probability distribution known as the prior distribution or prior.[26] This prior information is updated and synthesized with experimental data to establish so-called posterior distributions that can be used as the basis for inferential decisions.[27] The application of Bayesian inference in materials science is not entirely new, however, this work represents one of the first demonstrations of a Bayesian method to model the melt pool geometry with implications in additive manufacturing of metals and alloys.[28-30] Bayesian analysis can be seen as a process for obtaining predictions based on a range of assumptions about both prior distributions and likelihoods. These assumptions, however, require that reasoned justifications for the prior distribution and likelihood functions are made.

As a first step, the likelihood function, $P(M|\theta)$, is derived for the fitting of the modified E-T model. For a given dataset $M = \{x_1, \ldots, x_n\}$ of observed experimental melt pool depths, the likelihood function returns the sum of the probability densities of attaining each datum under the current model parameters represented by the vector θ. Simply put, it is the sum of the logarithmic probability densities of attaining the observed experimental depths with the current effective absorptivity and powder bed porosity values in the modified E-T model. Due to the large variability in melt pool measurements, the standard deviation in depths is chosen to be 15µm for the probability density calculation in the likelihood function. Although subjective, this value is informed by experiments and existing literature on the variability of measured depths for constant processing parameters.

The prior distribution, $P(\theta)$, is central to Bayesian analysis but remains controversial unless there is a physical mechanism to justify the choice. Due to the uncertainty surrounding accurate values for the absorptivity and porosity of powder beds, a weakly informative, subjective prior was used based on existing literature and the author's personal judgment. Prior distributions were specified for the absorptivity and powder bed porosity separately. The distributions were considered to be normal with specified mean and standard deviation values as shown in Table 2. The mean absorptivity value is chosen based on the work of Boley et al., who measured the absorptivity of different metal powders using powder calorimetric measurements under the laser conditions specific to that study.[13] The mean powder bed porosity value is chosen based on the theoretical limit of the random packing density of equal spheres being around 64%.[31] To ensure that the obtained values are theoretically possible, both prior distributions were constrained to be positive values less than unity. The posterior distributions are those that best fit the modified version of the E-T model to experimental data.

Table 2 Normal prior distribution mean and standard deviation values

Material	μ_{abs}	σ_{abs}	μ_{por}	σ_{por}
SS316L	0.68	0.15	0.40	0.10
Ti64	0.74	0.15	0.40	0.10
In718	0.67	0.15	0.40	0.10

The posterior density $P(\theta|M)$ expresses the updated belief about the parameters θ given the prior distribution and inclusion of data in the likelihood function.[10] In short, the posterior distribution represents the updated belief of the parameter values after collecting data and fitting the model. In practice, the posterior distributions are not determined by Bayes theorem, but by a computational method called Markov chain Monte Carlo (MCMC) sampling. Sampling algorithms are used to overcome the challenges of a multi-dimensional posterior by iteratively sampling a simpler proposal distribution.[27] For this paper, the Metropolis-Hastings algorithm was used to obtain samples from the posterior

distribution. The specifics of the algorithm are handled by the Bayesian Tools (BT) package in the R-language.[32] The initial samples of the algorithm may be biased by the starting value, so a burn-in of 1,000 samples was used. Additionally, the total number of iterations was set to 10,000 which was a large enough sample to guarantee convergence. Parallelization was necessary for this problem as a single modified E-T model run can take several minutes and this calculation is performed thousands of times. Once the posterior distributions for each parameter were determined from the Bayesian analysis, these input parameter distributions were forward propagated into the melt pool geometry predictions of the modified E-T model.

Results and Discussion

The effect of incorporating temperature dependent material properties and powder bed conditions on the melt pool geometry in the modified E-T model is shown by comparing Fig. 5 and Fig. 6. A comparison of melt pool depth predictions with the experimental data indicates that the modifications are still not significant enough to account for all the shortcomings of the E-T model in accurately predicting melt pool geometries, especially at higher powers where the keyhole regime is prevalent. This is an expected outcome when constant process parameters of effective absorptivity and powder bed porosity are used as inputs for the model, which is why the Bayesian analysis is utilized to fit these parameters to the modified E-T model based on the experimental observations.

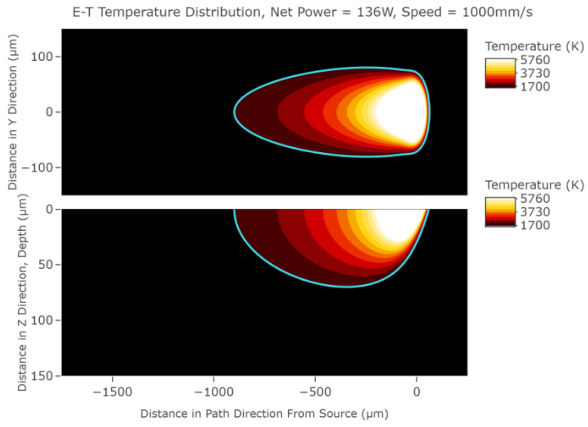

Fig. 5 Contour plot of the temperature distribution calculated for SS316L via the original E-T model at net laser power of 136W and scanning speed of 1000mm/s

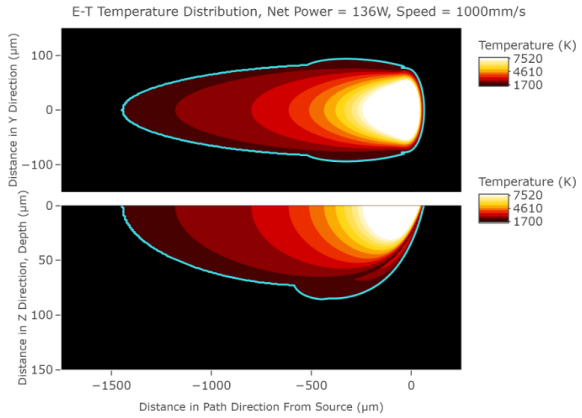

Fig. 6 Contour plot of the temperature distribution calculated for SS316L via the adapted E-T model for L-PBF at net laser power of 136W and scanning speed of 1000mm/s

Bayesian E-T Model

The Bayesian run output for two of the 316L stainless steel partitions is shown in Figs. 7 & 8. In Fig. 7, the average laser power and scan speed of the experimental data in the partition are 186 W and 1271 mm/s, respectively. While both the posterior density distributions of the effective absorptivity and porosity are concentrated at slightly lower values than the prior, they are relatively unchanged when contrasted with the output in Fig. 8, where the average laser power and scan speed of the partition are 243 W and 350 mm/s, respectively. In this higher power and lower speed partition, the posterior distributions are reflective of the keyholing phenomena where multiple laser reflections occur during the formation of a vapor column. Similar trends are seen for the three materials when comparing the direct Bayesian output of the high power, low speed partitions to the low power, high speed data partitions.

In the context of probabilistic calibration, the posterior distribution mean values and standard deviation can be introduced as the most plausible values for the model parameters and their standard deviations, respectively. The sampling process continues until the proposal distribution becomes stationary, which is equivalent to parameter convergence in conventional regression. The key functionality of Bayesian inference is that the MCMC parameter samples converge to a fixed distribution rather than a constant value as would be the case with simpler regression methods, which offers insight into applicability and uncertainty.

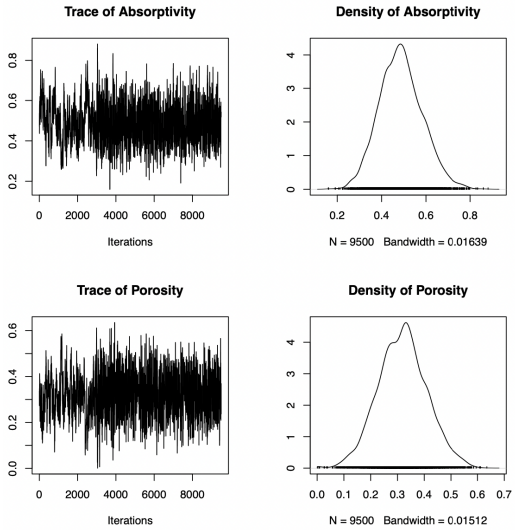

Fig. 7 Bayesian chain values and posterior probability density distributions for the SS316L partition with an average laser power of 186W and average scan speed of 1271 mm/s

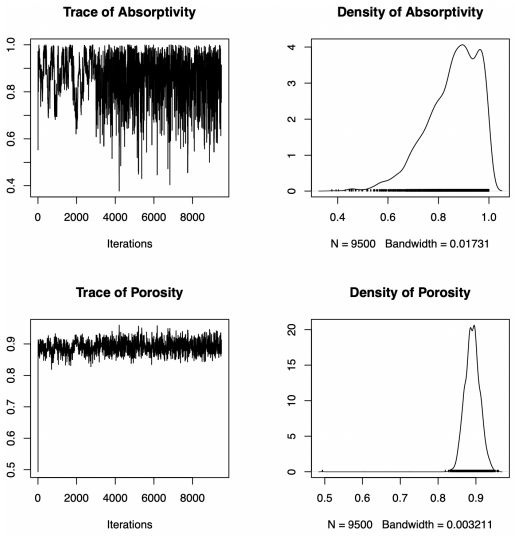

Fig. 8 Bayesian chain values and posterior probability density distributions for the SS316L partition with an average laser power of 243W and average scan speed of 350 mm/s

As a result of the experimental data partitioning scheme, the Bayesian inferred parameters are discrete throughout the P-V space and are taken to be located at the mean of the power and speed from the experimental data in the partition. However, it is desirable to be able to sample the entire P-V space in a continuous fashion to be able to predict melt pool geometries at all applicable process conditions. To resolve this issue, the mean values from the posterior distributions of each partition were used to fit a response surface for each parameter. This allows for continuous sampling at different process conditions. The response surfaces of the effective absorptivity and powder bed porosity parameters for each material are shown in Figs. 9-11.

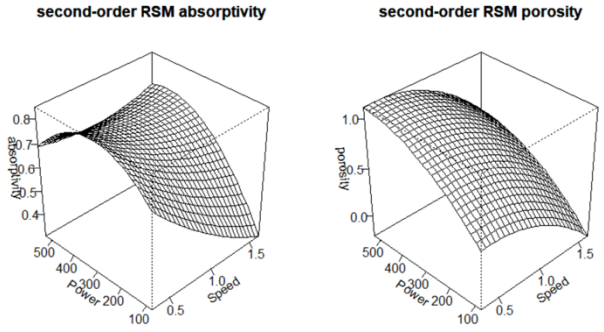

Fig. 9 Response surfaces fit to the mean values of the Bayesian posterior density distributions from each partition for SS 316L

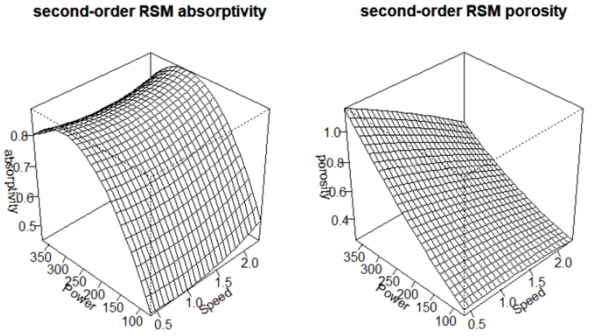

Fig. 10 Response surfaces fit to the mean values of the Bayesian posterior density distributions from each partition for Ti-6Al-4V

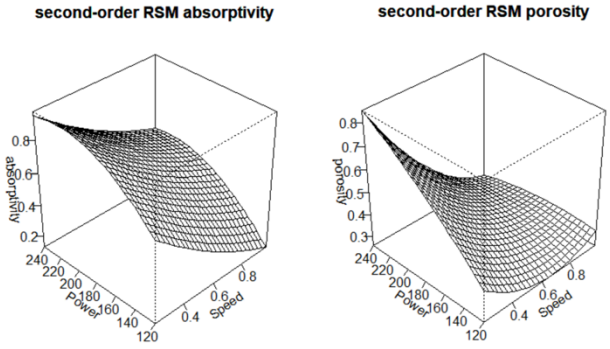

Fig. 11 Response surfaces fit to the mean values of the Bayesian posterior density distributions from each partition for Inconel 718

Similar trends in effective absorptivity and powder bed porosity are observed for all three materials, although some differences are noted due to the differences in the experimental data such as the range of power and speeds tested. As shown in the response surface plots, the effective absorptivity and porosity are both strongly influenced by laser power and speed. The response surfaces show generally increased effective absorptivity as power increases and speed decreases.

These trends are explained by physical mechanisms, such as evaporation, multiple reflection, and spattering. Boley et al. found that most practical materials have a low reflectivity and powder absorptivity that is 1.5-2 times that of the fat plate.[13] Trapp et al. performed similar experiments to determine the effect of laser power and speed on the absorptivity of metal powders and found that the onset of keyhole formation coincided with an increase in the absorption of the laser light.[12] The powder bed porosity is shown to increase as the laser power increases and speed decreases. Both of these trends are indicative of vapor column formation that becomes increasingly prevalent with the keyhole phenomenon at high power and low speed. During keyholing, the melt pool is further depressed due to recoil pressure, and in these experimental conditions, the pressure on the melt pool surface leads to the formation of a vapor column and deep melt pool penetration.[14]

In regard to the absorptivity, which can be measured by various means, the results agree with experimental evidence for low effective absorptivity of the solid/liquid phases and high effective absorptivity upon vaporization and keyhole formation.[12,13] Localized porosity as a result of the formation of a vapor column is harder to determine experimentally, but it can be understood that the formation of a vapor column acts to decrease the local powder bed packing and increase porosity. As identified by Cunningham et al., evaporation of the metal from the surface leads to the formation of vapor depressions at all relevant processing parameters.[14] As a result, the packing density below the laser spot can vary from that of the unaltered powder bed to that of a vapor column depending on the selected processing parameters.

Using the response surfaces to attain values for the effective absorptivity and powder bed porosity, melt pool geometries can be predicted using the Bayesian fit E-T model across the P-V space. In Figs. 12 & 13, a comparison is made of depths predicted with the conventional E-T model using constant parameter values typically used in literature and the Bayesian optimized parameter values from this work. The results show that the E-T model has generally good estimations of melt pool dimensions for the lack of fusion and conduction melting modes, but not for the depth prediction in the keyholing mode, where experimentally measured depths far exceed the model predictions. Since the physics associated with the keyholing phenomenon are not considered in the E-T model, the depth prediction is considerably underestimated for these experimental conditions leading to a lack of identification of the keyhole regime. The Bayesian approach shows greatly improved agreement with experiment across the process space.

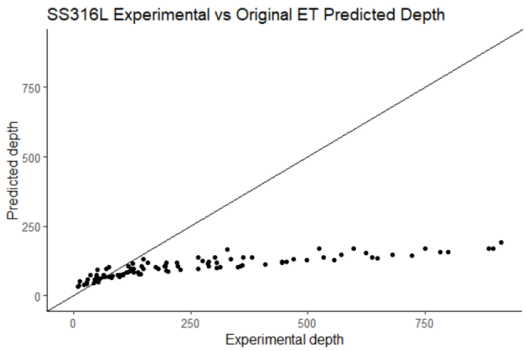

Fig. 12 Plot comparing original E-T model depth predictions with experimental single-track data

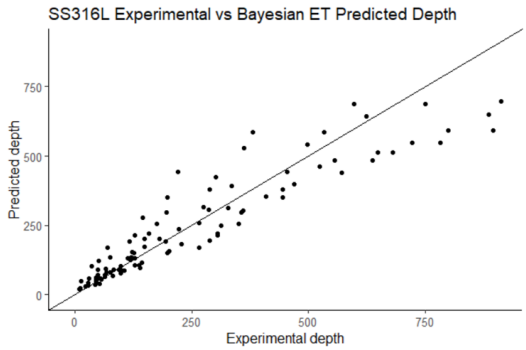

Fig. 13 Plot comparing Bayesian-fit modified E-T model depth predictions with experimental single-track data

Printability Maps

With the Bayesian fit parameters interpolated across the parameter space using response surface methodology, material specific printability maps can be constructed that illustrate regions of the process space where defects are prevalent and where optimal melt pool geometries can be attained. The three inputs to a printability map are the layer thickness (t), and the melt pool width (W) and depth (D) as functions of laser power and scan speed. Typically, the value for layer thickness is fixed and kept constant. Ratios of W/D and D/t are calculated across the parameter space from the Bayesian fit E-T model where input parameters vary as a function of laser power and scan speed. Regions of the process space where $W/D < 1.5$ and $D/t < 1.5$ are labeled as regions of keyholing and lack of fusion, respectively.[8] Balling was excluded from consideration as a distinct defect region. Any area not in the lack of fusion and keyhole regions is considered to be a viable option for the desired conduction mode of L-PBF. This exercise serves to validate the predictive power of the Bayesian approach.

Fig. 14 shows two printability maps for each material, where the first is created using the original E-T model and the second utilizes the Bayesian-fit modified E-T model. Both maps are created for a Gaussian laser distribution with beam diameter of 50 μm and layer

thickness of 30 µm. One of the striking differences is that the original E-T model, with constant material absorptivity and no powder bed conditions, fails to characterize any laser power scan speed parameter combination as part of the keyhole regime. Demonstrated in Fig. 12, this is a result of the original E-T model formulation being unable to predict melt pool depths at process conditions corresponding to keyhole phenomenon and is further shown here in the printability maps. This is a well-known deficiency of the E-T model when a constant value of absorptivity and solid material bed are assumed. In sharp contrast, the modified E-T model with Bayesian fit effective absorptivity and powder bed porosity parameters can predict both the keyhole and lack of fusion regions. These figures demonstrate the ability to establish bounds on the P-V process space that is unbounded by the original E-T model. Machine limitations would further bound the viable process conditions in the conduction region.

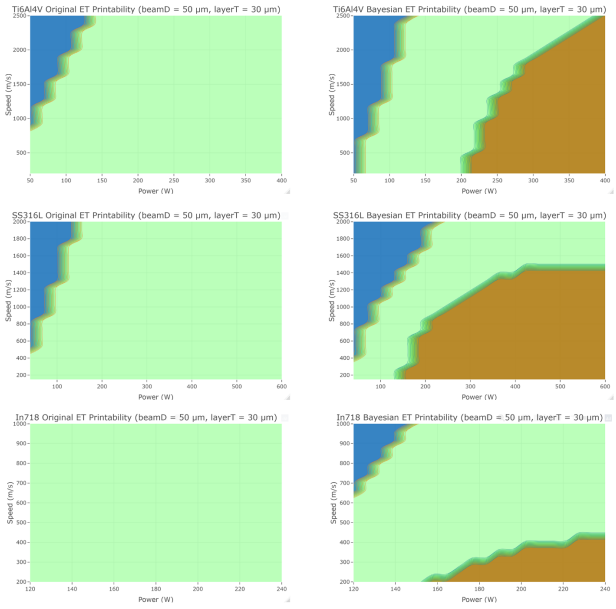

Fig. 14 Original E-T model (left) and Bayesian-fit modified E-T model (right) printability maps for the materials Ti-6Al-4V (top), 316L stainless steel (middle) and Inconel 718 (bottom)

Conclusion

This work provides insight into the applicability of an inexpensive analytical model in the analysis and design of L-PBF processes. Initially developed in the context of metal arc welding, the Eagar-Tsai model stands out among the most widely used and computationally cheap models to predict melt pool geometry characteristics. In this work, the original model formulation was modified by incorporating temperature dependent material properties and powder bed conditions to better represent the L-PBF process. The model was further improved by the use of Bayesian inference to calibrate power and speed dependent effective absorptivity and powder bed porosity values that agree with experiment. Although there is some uncertainty due to the missing physics and assumptions of the model, the model accuracy and trend are satisfactory for the purpose of accelerated process design and analysis. Importantly, the determination of material specific optimal process windows, or printability maps, based on geometric criteria can direct applications at the process space with the most desirable outcomes of L-PBF. Formation of the keyhole mode was detected for the three material systems investigated, which is a limitation inherent in the application of the original E-T model. The method put forth in this paper provides a principled approach for rapidly surveying the laser power and speed parameter space for any material with major implications in the additive manufacturing of metals and alloys.

Acknowledgements

This research was financially supported by the Virginia Space Grant Consortium (VSGC) Undergraduate STEM Research Scholarship Program as a project with relevance to NASA and the future of aerospace. Additionally, this work would not have been possible without the exceptional support of my advisor, Dr. Prasanna Balachandran, whose guidance and expertise proved vital throughout the project. Finally, I would like to acknowledge the Materials Informatics Group at UVA for their assistance, encouragement and useful critique along the way.

References

[1] Kamath C (2016) Data mining and statistical inference in selective laser melting. Int J Adv Manuf Technol 86:1659. https://doi.org/10.1007/s00170-015-8289-2

[2] Bassoli E, Sola A, Celesti M, Calcagnile S, Cavallini C (2018) Development of laser-based powder bed fusion process parameters and scanning strategy for new metal alloy grades: a holistic method formulation. Materials 11:2356. https://doi.org/10.3390/ma11122356

[3] Johnson L, Mahmoudi M, Zhang B, Seede R, Huang X, Maier JT, Maier HJ, Karaman I, Elwany A, Arróyave R (2019) Assessing printability maps in additive manufacturing of metal alloys. Acta Materialia 176:199. https://doi.org/10.1016/j.actamat.2019.07.005

[4] Seede R, Shoukr D, Zhang B, Whitt A, Gibbons S, Flater P, Elwany A, Arróyave R, Karaman I (2020) An ultra-high strength martensitic steel fabricated using selective laser melting additive manufacturing: densification, microstructure, and mechanical properties. Acta Materialia 186:199. https://doi.org/10.1016/j.actamat.2019.12.037

[5] Chen Y, Wang H, Wu Y, Wang H (2020) Predicting the printability in selective laser melting with a supervised machine learning method. Materials 13:5063. https://doi.org/10.3390/ma13225063

[6] Tan JH, Wong WLE, Dalgarno KW (2017) An overview of powder granulometry on feedstock and part performance in the selective laser melting process. Addit Manuf 18:228. https://doi.org/10.1016/j.addma.2017.10.011

[7] Eagar TW, Tsai NS (1983) Temperature fields produced by traveling distributed heat sources. Weld Res Suppl 62:346–355

[8] Carter MJ, El-Desouky A, Andre MA, Bardet P, LeBlanc S (2019) Pulsed laser melting of bismuth telluride thermoelectric

materials. J Manuf Process 43:35. https://doi.org/10.1016/j.jmapro.2019.04.021
[9] Mondal S, Gwynn D, Ray A, Basak A (2020) Investigation of melt pool geometry control in additive manufacturing using hybrid modeling. Metals 10(5):683. https://doi.org/10.3390/met10050683
[10] Bertoli US, Wolfer AJ, Matthews MJ, Delplanque JPR, Schoenung JM (2017) On the limitations of volumetric energy density as a design parameter for selective laser melting. Mater Des 113:331. https://doi.org/10.1016/j.matdes.2016.10.037
[11] Hamada MS, Higdon DM, Abes J, Hills C, Peters AM (2015) Illustrating how science can be incorporated into a nonlinear regression model. Quality Eng 27(4):416. https://doi.org/10.1080/ 08982112.2015.1023314
[12] Trapp J, Rubenchik AM, Guss G, Matthews MJ (2017) In situ absorptivity measurements of metallic powders during laser powder-bed fusion additive manufacturing. Appl Mater Today 9:341. https://doi.org/10.1016/j.apmt.2017.08.006
[13] Boley CD, Mitchell SC, Rubenchik AM, Wu SSQ (2016) Metal powder absorptivity: modeling and experiment. Appl Opt 55(23):6496. https://doi.org/10.1364/AO.55.006496
[14] Cunningham R, Zhao C, Parab N, Kantzos C, Pauza J, Fezzaa K, Sun T, Rollett AD (2019) Keyhole threshold and morphology in laser melting revealed by ultrahigh-speed x-ray imaging. Science 363(6429):849. https://doi.org/10.1126/science.aav4687
[15] Rubenchik A, Wu S, Mitchell S, Golosker I, LeBlanc M, Peterson N (2015) Direct measurements of temperature-dependent laser absorptivity of metal powders. Appl Opt 54(24):7230. https://doi.org/10.1364/AO.54.007230
[16] King WE, Anderson AT, Ferencz RM, Hodge NE, Kamath C, Khairallah SA, Rubenchik AM (2015) Laser powder bed fusion additive manufacturing of metals; physics, computational, and materials challenges. Appl Phys Rev 2(4):041304. https://doi.org/10.1063/1.4937809
[17] Pal R (2008) On the Lewis–Nielsen model for thermal/electrical conductivity of composites. Compos Part A Appl Sci Manuf 39(5):718. https://doi.org/10.1016/j.compositesa.2008.02.008
[18] Rammos P (2020) Numerical framework for selective laser melting processing of thermoelectric materials. Master's thesis, George Washington University (2020)
[19] Hu Z, Nagarajan B, Song X, Huang R, Zhai W, Wei J (2019) Formation of SS316L single tracks in micro selective laser melting: surface, geometry, and defects. Adv Mater Sci Eng 2019:9451406. https://doi.org/10.1155/2019/9451406
[20] Goosens L, Hooreweder BV (2021) A virtual sensing approach for monitoring melt-pool dimensions using high speed coaxial imaging during laser powder bed fusion of metals. Addit Manuf 40:101923. https://doi.org/10.1016/j.addma.2021.101923
[21] Lee S, Peng J, Shin D, Choi YS (2019) Data analytics approach for melt-pool geometries in metal additive manufacturing. Sci Tech Adv Mater 20(1):359. https://doi.org/10.1080/14686996.2019.1671140
[22] Vaglio E, De Monte T, Lanzutti A, Totis G, Sortino M, Fedrizzi L (2020) Single tracks data obtained by selective laser melting of Ti6Al4V with a small laser spot diameter. Data in Brief 33:106443. https://doi.org/10.1016/j.dib.2020.106443
[23] Kusuma C (2016) The effect of laser power and scan speed on melt pool characteristics of pure titanium and Ti-6Al-4V alloy for selective laser melting. Master's thesis, Wright State University (2016)
[24] Dilip JJS, Zhang S, Teng C, Zeng K, Robinson C, Pal D, Stucker B (2017) Influence of processing parameters on the evolution of melt pool, porosity, and microstructures in Ti-6Al-4V alloy parts fabricated by selective laser melting. Prog Addit Manuf 2:157. https://doi.org/10.1007/s40964-017-0030-2
[25] Patel S, Vlasea M (2020) Melting modes in laser powder bed fusion. Materialia 9:100591. https://doi.org/10.1016/j.mtla.2020.100591
[26] Bayes T (1763) LII. An essay towards solving a problem in the doctrine of chances. Philos Trans R Soc Lond 53:370. https://doi.org/10.1098/rstl.1763.0053
[27] Spiegelhalter D, Rice K (2009) Bayesian statistics. Scholarpedia 4(8):5230. https://doi.org/10.4249/scholarpedia.5230 (Revision 185711)
[28] Xue D, Balachandran PV, Yuan R, Hu T, Qian X, Dougherty ER, Lookman T (2016) Accelerated search for BaTiO3-based piezoelectrics with vertical morphotropic phase boundary using Bayesian learning. Proc Natl Acad Sci 113(47):13301. https://doi.org/ 10.1073/pnas.1607412113
[29] Fancher CM, Han Z, Levin I, Page K, Reich BJ, Smith RC, Wilson AG, Jones JL (2016) Use of Bayesian inference in crystallographic structure refinement via full diffraction profile analysis. Sci Rep 6(1):31625. https://doi.org/10.1038/srep31625
[30] Kim H, Inoue J, Kasuya T, Okada M, Nagata K (2020) Bayesian inference of ferrite transformation kinetics from dilatometric measurement. Comput Mater Sci 184:109837. https://doi.org/10.1016/j.commatsci.2020.109837
[31] Zhu H, Fuh J, Lu L (2007) The influence of powder apparent density on the density in direct laser-sintered metallic parts. Int J Mach Tools Manuf 47(2):294. https://doi.org/10.1016/j.ijmachtools.2006.03.019
[32] Hartig F, Minunno F, Paul S (2019) BayesianTools: general-purpose MCMC and SMC samplers and tools for Bayesian statistics. https://CRAN.R-project.org/package=BayesianTools. R package version 0.1.7